

Silicon solar cell with undoped tin oxide transparent electrode

Received: 10 January 2023

Accepted: 7 July 2023

Published online: 07 August 2023



Cao Yu^{1,8}, Qiaojiao Zou^{2,3,4,5,6,8}, Qi Wang¹, Yu Zhao¹, Xiaochao Ran¹, Gangqiang Dong¹✉, Chen-Wei Peng¹, Vince Allen⁷, Xinming Cao¹, Jian Zhou¹, Ying Zhao^{2,3,4,5,6} & Xiaodan Zhang^{2,3,4,5,6}✉

Silicon heterojunction (SHJ) solar cells are one of the most promising directions in the future photovoltaic industry. The limited supply of rare indium and the high cost of silver paste are among the most important problems that SHJ solar cells will face. To overcome the obstacle of indium-based transparent electrodes for efficient SHJ solar cells, here we successfully prepared cheap and mass-producible undoped tin oxide (SnO_x) electrode materials by sputtering at room temperature. Taking advantage of its natural oxygen vacancy defect, the carrier mobility and resistivity of prepared materials reached $22 \text{ cm}^2 \text{ V}^{-1} \text{ s}^{-1}$ and $2.38 \times 10^{-3} \Omega \text{ cm}$, respectively. The SHJ solar cell with an undoped SnO_x front transparent electrode demonstrated an efficiency of 24.91%. Furthermore, SnO_x films have excellent chemical stability and can withstand corrosion by acid and alkali solutions during electroplating processes. Finally, SHJ solar cells with plating copper electrode and double-sided indium-based transparent electrodes halved were prepared, and a certified efficiency of 25.94% (total area of 274.4 cm^2) was achieved.

Low-cost and highly efficient solar cells are vital for achieving the goal of carbon neutralization. Silicon heterojunction (SHJ) solar cells have become a research hotspot in the photovoltaic field because of their high conversion efficiency and low temperature coefficient¹. Presently, SHJ solar cells with interdigitated back contacts have reached power conversion efficiencies >26% (ref. 2). However, the expensive indium-based transparent electrodes (TEs) and silver metal electrodes limit their large-scale applications in the future³. Therefore, it is imperative to largely reduce the consumption of indium-based TEs and silver to achieve the target output for sustainable multi-terawatt scale manufacturing.

Materials such as aluminium-doped zinc oxide (AZO) and boron-doped zinc oxide have been selected to partially replace the need for indium-based TEs, achieving an efficiency of 23.90%

(bifacial cell with indium tin oxide (ITO)/AZO/ITO front TE and AZO rear TE)⁴ and 16.60% (bifacial cell with ITO front TE and boron-doped zinc oxide rear TE)⁵, respectively. However, this remains a far cry from the performance of current SHJ solar cells based on indium-based TEs. Besides, if the electrodes are prepared using electroplating processes, the acid and alkali resistance of TEs must be considered⁶. ZnO-based materials developed so far are not very resistant to corrosion⁷.

Undoped SnO_x thin films fabricated by solution and atom layer deposition have been widely investigated for perovskite^{8,9}, silicon^{10,11} and perovskite/silicon tandem solar cells^{12,13} as a selective carrier transport layer or an anti-ion-bombardment buffer layer, respectively. Up to now, there are almost no reports on the use of TEs in solar cells.

Here, sputtering, widely used for SHJ solar cells and therefore a compatible deposition technology for commercialization, was

¹Suzhou Maxwell Technologies Co., Ltd., Suzhou, P. R. China. ²Institute of Photoelectronic Thin Film Devices and Technology, Renewable Energy Conversion and Storage Center, Solar Energy Research Center, Nankai University, Tianjin, P. R. China. ³Haihe Laboratory of Sustainable Chemical Transformations, Tianjin, P. R. China. ⁴Key Laboratory of Photoelectronic Thin Film Devices and Technology of Tianjin, Tianjin, P. R. China. ⁵Engineering Research Center of Thin Film Photoelectronic Technology of Ministry of Education, Tianjin, P. R. China. ⁶Collaborative Innovation Center of Chemical Science and Engineering (Tianjin), Tianjin, P. R. China. ⁷Sundrive Solar Pty., Ltd., Kirrawee, New South Wales, Australia. ⁸These authors contributed equally: Cao Yu, Qiaojiao Zou. ✉e-mail: gqdong@maxwell-gp.com.cn; xdzhang@nankai.edu.cn

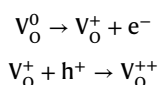
applied to fabricate undoped SnO_x TEs. The undoped SnO_x film has a low absorption coefficient of $2.14 \times 10^5 \text{ cm}^{-1}$ at 600 nm. The carrier mobility and resistivity of the prepared materials reach $22 \text{ cm}^2 \text{ V}^{-1} \text{ s}^{-1}$ and $2.38 \times 10^{-3} \Omega \text{ cm}$, respectively. We replaced the front TEs in SHJ solar cells with undoped SnO_x films, and an efficiency of 24.91% was obtained. We also reduced the contact resistance with n- $\mu\text{c-SiO}_x\text{:H}$ by means of hydrogenated transition metal-doped indium oxide (IMO:H)+ SnO_x bilayer films, which facilitates the enhancement of the fill factor (FF) and further improves the performance of the SHJ solar cells. In addition, it was verified that the IMO:H+ SnO_x bilayer films have good resistance to acid and alkali corrosion. Finally, a certified efficiency of 25.94% (total area of 274.4 cm^2) was achieved by applying the IMO:H+ SnO_x bilayer films combined with the copper electroplating process for SHJ solar cells.

SnO_x film and SHJ solar cells

The properties of the undoped SnO_x films deposited under different process conditions are shown in Supplementary Fig. 1 and Supplementary Table 1. We obtained good-quality undoped SnO_x films by adjusting the deposition process (Supplementary Table 2). Among them, the film with the best opto-electrical properties showed a resistivity of $2.38 \times 10^{-3} \Omega \text{ cm}$, a mobility of $22 \text{ cm}^2 \text{ V}^{-1} \text{ s}^{-1}$, a carrier concentration of $1.02 \times 10^{20} \text{ cm}^{-3}$ and a low absorption coefficient of $2.14 \times 10^5 \text{ cm}^{-1}$ at 600 nm (Figs. 1a,b). The X-ray diffraction (XRD) characterization in Fig. 1c shows that the SnO_x films have no characteristic peaks and appear amorphous, resulting in low surface roughness as seen by atomic force microscopy (AFM) (Fig. 1c, inset).

X-ray photoelectron spectroscopy (XPS) measurements were performed to confirm the chemical composition of the films further. Figure 1d illustrates the typical core-level spectra of Sn 3d and O 1s. The Sn 3d spectrum depicts two spin-orbit double peaks belonging to Sn^{4+} and Sn^{2+} respectively, where Sn^{4+} is located at 486.9 eV ($\text{Sn}^{4+} 3d_{5/2}$) and 495.3 eV ($\text{Sn}^{4+} 3d_{3/2}$), and Sn^{2+} is located at 486.2 eV ($\text{Sn}^{2+} 3d_{5/2}$) and 494.6 eV ($\text{Sn}^{2+} 3d_{3/2}$). In addition, the peak positions of Sn^{4+} and Sn^{2+} are separated by 0.7 eV and the gap between the Sn $3d_{5/2}$ and Sn $3d_{3/2}$ levels (8.4 eV) is essentially the same as in the standard spectrum of Sn. Furthermore, the O 1s peak can be fitted to two peaks, located at 530.05 eV and 530.72 eV, assigned to O– Sn^{2+} and O– Sn^{4+} , respectively. The binding energies of all the components in this work are consistent with previously reported values^{14,15}. The proportions of different species are presented in Supplementary Table 3. Quantification of the Sn 3d and O 1s peaks provides an average O/Sn atomic ratio of 1.81. This signifies the highly oxygen-deficient non-stoichiometric formation of the SnO_x film, which is why it can conduct electricity.

The photoluminescence (PL) emission spectra of SnO_x films are shown in Fig. 1e. The emission spectrum can be deconvoluted by Gaussian fitting into five peaks, centred at 366, 399, 448, 500 and 528 nm. As the band gap of SnO_x films is approximately 3.7–3.9 eV, these emission peaks are mainly caused by various defects in the films. Among them, the origin of the emission peak at 399 nm is thought to be related to an oxygen vacancy¹⁶. Generally, there are three kinds of oxygen vacancies in SnO_x films: V_{O}^0 (without any positive charges), V_{O}^+ (with a positive charge) and V_{O}^{++} (with two positive charges)¹⁷. The following relationship exists between them:



At room temperature, V_{O}^0 centres dissociate into V_{O}^+ centres and conduction band electrons. V_{O}^+ can combine with electrons shared by neighbouring Sn^{4+} , and the energy level of V_{O}^+ is close to the conduction band, so the emission peak at 399 nm corresponds to the electron transition from V_{O}^+ donor levels to the valence band. At the same time, V_{O}^+ can easily trap holes in the valence band to form V_{O}^{++} .

As demonstrated by band structure calculations, the oxygen vacancies lead to a fully occupied flat energy level at about 1 eV above the top valence band and an empty energy level in resonance with the conduction band¹⁸. Thus, the PL peak at 448 nm can be attributed to the electron transition from the conduction band minimum to the V_{O}^{++} energy level. The origin of the peak at 500 nm is not entirely clear, but according to other reports available, it may be related to the electron transition from the conduction band minimum to the V_{Sn} energy level¹⁹. A schematic representation of the above defect levels and emission routes is given in Supplementary Fig. 2.

The XPS study confirms the highly oxygen-deficient non-stoichiometric formation of the SnO_x film deposited at room temperature. The room temperature PL emission at 399 nm and 448 nm were dominated by the oxygen vacancies. The above results explain the outstanding electrical properties of the SnO_x films. Subsequently, the optimized SnO_x thin films were applied to traditional SHJ solar cells as the front TE layer, replacing IMO:H to reduce the metal indium content. The structure of the SHJ solar cells is shown in Fig. 1f (inset). A total of nine SHJ solar cells of M6 size were prepared (Supplementary Fig. 3), with an average efficiency of 24.83%, while the highest efficiency was 24.91% (open-circuit voltage, $V_{\text{oc}} = 747.7 \text{ mV}$; short-circuit current density, $J_{\text{sc}} = 39.60 \text{ mA cm}^{-2}$; FF = 84.14%) (Fig. 1f). The efficiency obtained in this work is at the leading edge compared with existing research on SHJ solar cells based on non- In_2O_3 TE materials^{5,20}. This work shows that undoped SnO_x films can be used as a window TE layer in SHJ solar cells, providing a reliable option to reduce the production cost of SHJ solar cells.

IMO:H+ SnO_x bilayer film and SHJ solar cells

A satisfactory efficiency was obtained when using SnO_x to replace IMO:H as the front TE layer in SHJ solar cells. However, we found that there was still a tiny difference of less than 1% compared with the non-replaced cell with an efficiency of 25.84% (Supplementary Fig. 4). The difference is mainly in the FF and J_{sc} . The average absorbance of SnO_x (0.94%) is slightly larger than that of IMO:H (0.67%) in the wavelength range of 400–1200 nm (Supplementary Fig. 5a), especially in the short wavelength region. In addition, the band gap of SnO_x (3.860 eV) is slightly smaller than that of IMO:H (3.897 eV), as can be understood from the Tauc plot (Supplementary Fig. 5b), so the transmission of light in the short wavelength region is also limited. In addition, the contact resistivity (ρ_c) between TEs and n- $\mu\text{c-SiO}_x\text{:H}$ is also an essential parameter for the performance of SHJ solar cells. The Cox and Strack configuration was used to measure ρ_c . See our previous work for details of the principle²¹. The ρ_c between SnO_x and IMO:H with n- $\mu\text{c-SiO}_x\text{:H}$, respectively, were studied. The structures of the devices are shown in Supplementary Fig. 6a. ρ_c is the slope of $(R_t - R_s)$ with respect to the curve of $4(\pi d^2) - 1$ according to this principle. The fitting results are shown in Supplementary Fig. 6b. The ρ_c between the SnO_x and n- $\mu\text{c-SiO}_x\text{:H}$ is $156.3 \text{ m}\Omega \text{ cm}^2$, which is much greater than that between IMO:H and n- $\mu\text{c-SiO}_x\text{:H}$ ($23.3 \text{ m}\Omega \text{ cm}^2$) (Supplementary Table 4). As a result, the large ρ_c between SnO_x and n- $\mu\text{c-SiO}_x\text{:H}$ is also an important reason for the reduced performance of SHJ solar cells with front SnO_x TEs.

Therefore, to further improve the efficiency, we designed IMO:H+ SnO_x bilayer thin films to increase the electrical conductivity of the films. For the IMO:H+ SnO_x bilayer films on glass substrate, the thickness ratio of IMO:H and SnO_x layers is 1:1, while maintaining a total bilayer thickness of 100 nm. The bilayer thin film has good optical properties with an absorption coefficient of $1.94 \times 10^5 \text{ cm}^{-1}$ at 600 nm (Supplementary Fig. 7). As can be seen from the XRD results in Fig. 2a, the crystalline orientation of the bilayer films was the same as that of IMO:H, and no characteristic peaks of SnO_x were found. Therefore, the bilayer film combines an amorphous SnO_x film and a polycrystalline IMO:H film. However, the crystallization peak strength of the bilayer film is weaker because the IMO:H film thickness is halved. In addition,

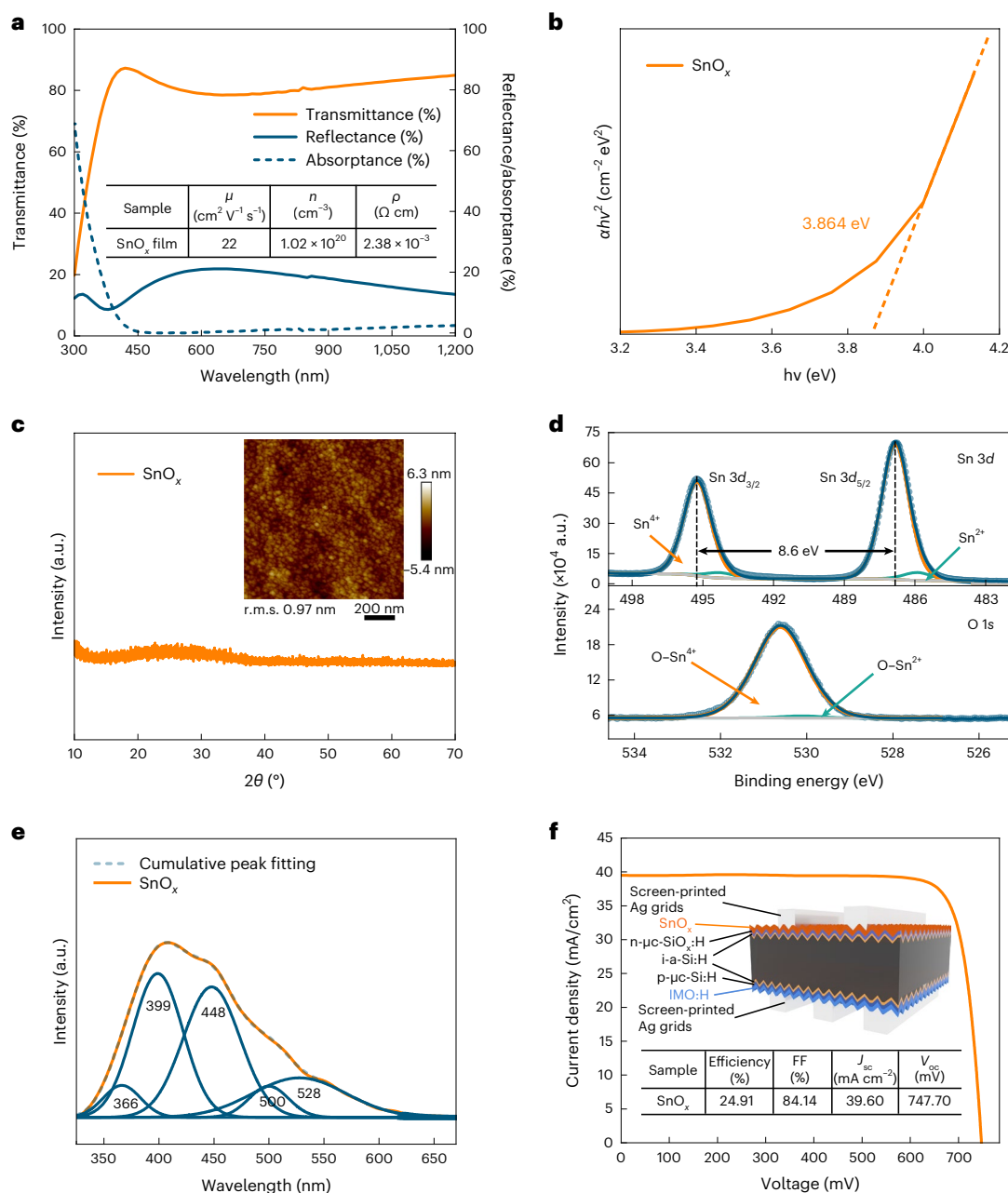


Fig. 1 | Material properties of undoped SnO_x films and application in SHJ solar cells. a–e, Optical characteristics (a), Tauc plot (b), XRD pattern (with inset AFM image) (c), element Sn 3d and O 1s XPS spectra (d) and PL emission spectra (e) of the SnO_x thin films. f, The J – V characteristic (with inset schematic illustration)

of the champion SHJ solar cell with an SnO_x film front TE. The dashed line in b is tangent to the curve, and the dashed line in d is a guide to the eye. The orange and green curves in d and blue curves in e are obtained by Gaussian fitting.

the surface roughness of the bilayer films is smaller than that of the polycrystalline IMO:H films (Supplementary Fig. 8), which is because the upper part of the bilayer films is amorphous SnO_x film with a smooth surface. This is consistent with the XRD pattern. Compared with a single layer of SnO_x film, the bilayer film has a threefold increase in mobility and an increase in carrier concentration, reducing the resistivity of the bilayer films (Fig. 2b). The bilayer films retain both the good optical properties of the SnO_x film and the excellent electrical properties of the IMO:H that ultimately exhibits better optical and electrical properties. In addition, considering that the films, as TEs, also need to have good stability in SHJ solar cells, we monitored the damp-heat (85 °C and 85% humidity) stability (Supplementary Table 5) and thermal (200 °C) stability (Supplementary Fig. 9) of SnO_x /IMO:H

and IMO:H/ SnO_x bilayer films. The results show that the parameters of SnO_x and IMO:H/ SnO_x bilayer films change little after damp-heat and thermal annealing treatment. Compared with IMO:H, which has been widely used in industrialization, the stability of SnO_x and IMO:H/ SnO_x bilayer films is not poor.

On the basis of the above improvements in film performance, we applied the bilayer film to SHJ solar cells by replacing the front TE. The structure is shown in Fig. 2c. Because of the above properties, all the performance parameters of the solar cells were improved, especially the FF, compared with the SnO_x monolayer film, which was attributed to the improved electrical and contact performance. Finally, a 25.71% ($V_{oc} = 748.34$ mV, $J_{sc} = 39.98$ mA cm^{-2} , FF = 85.95%) efficiency SHJ solar cell was achieved (Fig. 2c,d).

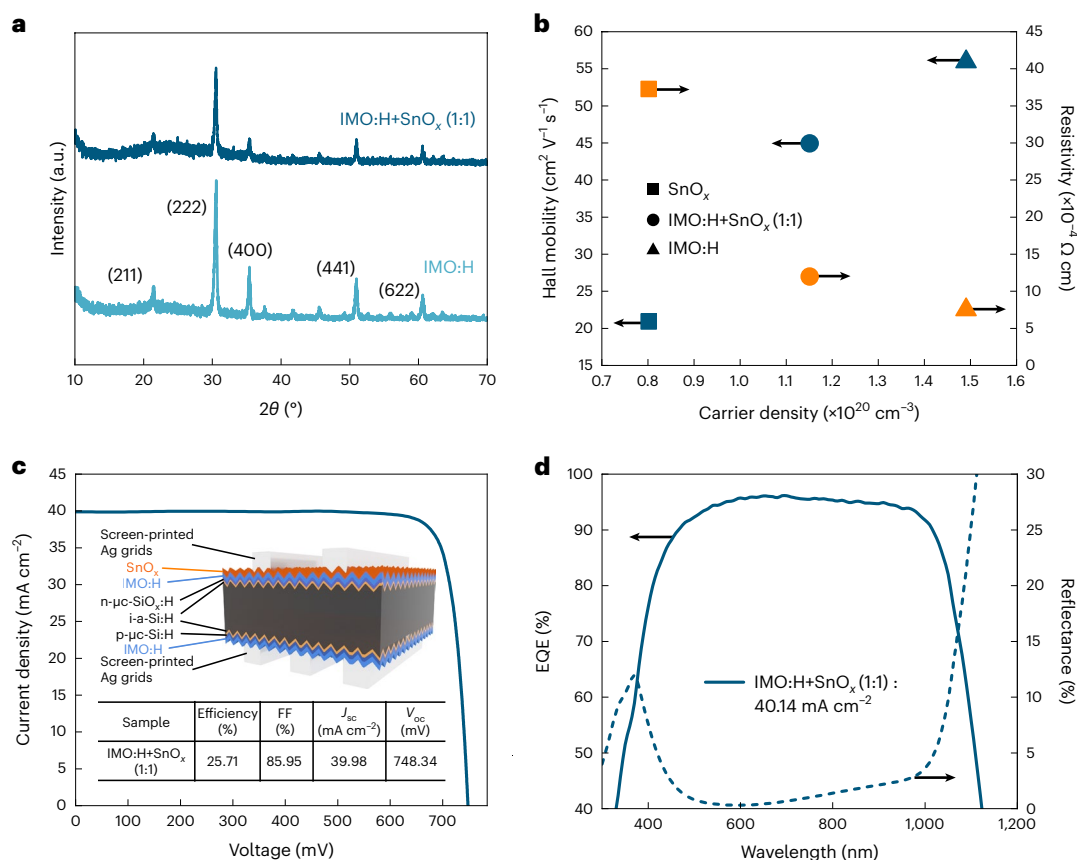


Fig. 2 | Material properties of IMO:H+SnO_x bilayer film and application in SHJ solar cells. a, XRD patterns of IMO:H and bilayer films. **b**, Electrical characteristics of SnO_x, IMO:H and bilayer films. **c, d**, J - V characteristic (**c**) and full-area external quantum efficiency (EQE) (**d**) of the champion SHJ solar cell

with an IMO:H+SnO_x bilayer film as front TE. The inset and table in **c** show a schematic illustration and the performance parameters of the champion solar cell, respectively. These arrows in **b** and **d** are guides to the eye.

To further reduce the indium content and the production costs, we replaced the TEs on both sides of the SHJ solar cell with IMO:H+SnO_x bilayer films. The cell structure is shown in Supplementary Fig. 10a. As with the replacement of the front TE with a single layer of SnO_x film, the indium content of the solar cell is also reduced by 50%, while the efficiency is further improved up to 25.64% (V_{oc} = 748.53 mV, J_{sc} = 40.05 mA cm⁻², FF = 85.51%) (Supplementary Fig. 10a,b). The improved electrical properties of the bilayer film resulted in an obvious improvement in FF (Supplementary Fig. 11 and Supplementary Tables 6, 7), further narrowing the performance gap versus solar cells without replacement of the indium-based TEs, from 0.93% to 0.20%. In addition, we also monitored the stability of these solar cells (Supplementary Fig. 12). It can be seen that, after 90 days of placement and subsequent high intensity light treatment (80 suns, over 200 °C), cells with IMO:H+SnO_x bilayer films as double-sided TEs still retained high efficiency with almost no decay, which is as good as the stability of the standard cells with IMO:H TEs.

Highly efficient and low-cost SHJ solar cells

To further reduce the cost, the metal electrodes of solar cells were prepared using the electroplating process, replacing silver with copper. As the electroplating process requires plating and stripping processes²², the SHJ solar cells will then be subjected to strong acid plating solution and alkali stripping solution. To test whether the bilayer films can withstand acid and alkali attack, the bilayer films deposited on glass substrates were immersed in plating solution and stripping solution, respectively (Supplementary Fig. 13). After corrosion by the plating and stripping solution, the opto-electrical properties of the bilayer material

hardly changed obviously (Supplementary Fig. 14). Compared with IMO:H, the bilayer material was relatively more stable (Supplementary Tables 8 and 9). Subsequently, we immersed the prepared complete SHJ solar cells also in the plating and stripping solution respectively (Supplementary Fig. 15). The solar cells showed no apparent damage before and after corrosion (Supplementary Fig. 16). After testing, it was found that all the performance parameters of the SHJ solar cells remained virtually unchanged before and after corrosion (Fig. 3a and Supplementary Table 10). Moreover, the contact performance between IMO:H+SnO_x and metal electrodes is almost the same as that between IMO:H and metal electrodes (Supplementary Table 11). On this basis, a highly efficient SHJ solar cell was prepared by replacing the silver electrode with a copper electrode, using an electroplating process (Fig. 3b). Subsequently, a champion efficiency of 25.94% (V_{oc} = 747.5 mV, J_{sc} = 40.49 mA cm⁻², FF = 85.71%) was achieved for the SHJ solar cell with a MgF₂ + SnO_x + IMO:H + n-μc-SiO_x:H front contact layer and a p-μc-Si:H + IMO:H + SnO_x rear contact layer (Fig. 3c), which achieved the Institut für Solarenergieforschung CalTeC performance certification. This result is at the forefront of previous studies on SHJ solar cells based on indium-less TEs (Supplementary Table 12) or electroplated copper electrodes (Supplementary Table 13).

This work demonstrates the feasibility of amorphous undoped SnO_x TEs with copper electrodes as an alternative to indium-based TEs with silver electrodes, which provides an effective solution to address the high cost of silver paste and limited supply of rare indium. We believe that such amorphous undoped SnO_x TEs that can be processed at room temperature are not only suitable for silicon solar cells but also perovskite and corresponding tandem devices. In addition, the

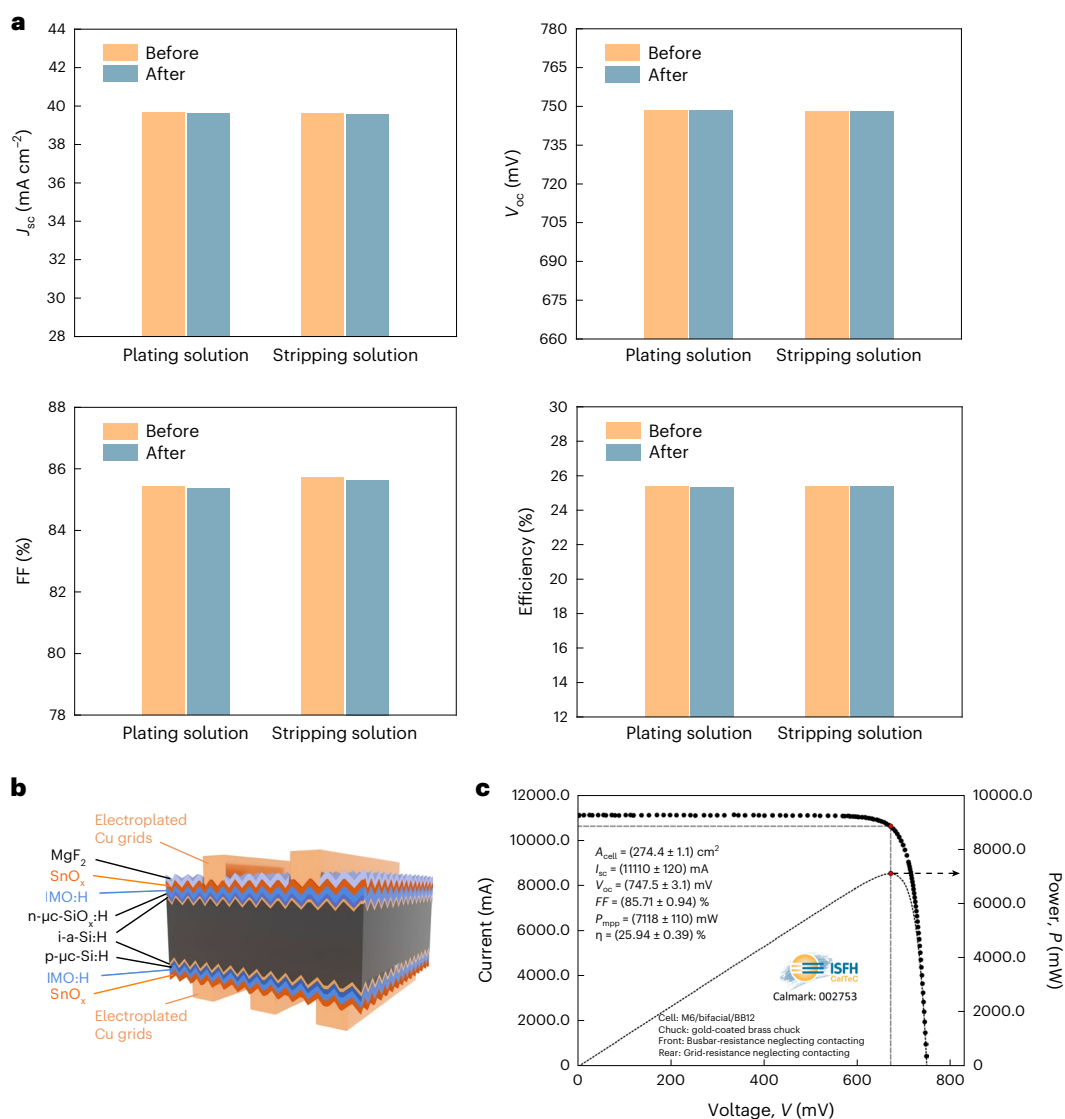


Fig. 3 | Chemical stability and low-cost efficient SHJ solar cells. a, Photovoltaic parameters of the SHJ solar cells with double 1:1 bilayer films before and after corrosion. **b, c**, Schematic illustration (**b**) and the light I - V curves (**c**) of the champion SHJ solar cell with double 1:1 bilayer films and copper electrodes.

SnO_x -derived materials are expected to have an attractive role in the fields of photoelectrocatalytic carbon dioxide reduction and hydrogen evolution by water splitting.

Methods

Transparent conductive oxide

Transparent conductive oxide (TCO) films were deposited by magnetron sputtering on textured silicon (100) wafers or glass substrates. SnO_2 planar ceramic targets with a target size of 1,000 mm (length) \times 125 mm (width) \times 9 mm (thickness) were used to prepare amorphous SnO_x films. The oxygen concentration can be tuned by adjusting the gas ratio of pure argon and pure oxygen during the deposition process. The base vacuum pressure in the chamber was 2×10^{-4} Pa, and the pressure during the sputtering process was set at 0.4–0.7 Pa. No additional heating was applied to the substrate during the deposition process. The films were deposited using radio-frequency (RF), direct current (DC) or DC + RF. The DC + RF mode refers to a dual power control sputtering method. During sputtering, both direct and alternating voltages are applied between the cathode and anode, and the parameters of the two power modes can be adjusted independently.

Indium oxide targets doped with transition metals were used to prepare IMO:H films, where M refers to three transition metal oxides of titanium oxide, cerium oxide and tantalum oxide. More details regarding the deposition process for IMO:H films can be found in previous work²¹. A bilayer film means the combination of SnO_x and IMO:H films in a 1:1 thickness ratio, with the total thickness of the layer remaining unchanged. Note that the sputtering of the IMO:H layers was always done before the deposition of the SnO_x layers.

SHJ solar cells

The equipment used in the solar cell preparation process in this paper is all home-made (including the equipment used in texturing and cleaning, chemical vapour deposition, physical vapour deposition and screen printing). The solar cells were fabricated as follows. First, commercial n-type (100)-oriented Czochralski silicon wafers with a thickness of 150 μm and resistivity of 1 $\Omega \text{ cm}$ were subjected to wet chemical treatment. Afterwards, 7 nm i-a-Si:H was deposited on both sides of the wafer as a passivation layer. Subsequently, 25 nm n- $\mu\text{c-SiO}_x\text{:H}$ and 36 nm p- $\mu\text{c-Si:H}$ were deposited as the front contact layer and rear emitter, respectively. Finally, TEs were deposited on both sides of the

sample (the deposition parameters and properties of the TEs that will eventually be used for device integration are shown in Supplementary Table 14), and then silver grids were printed on both sides. After screen printing, the solar cells were annealed at 200 °C for 20 min. The copper electrodes of the champion solar cell were prepared at SunDrive by bias-assisted light-induced plating. The plating duration was set to 10 min, resulting in an average deposited contact height of $13 \pm 1 \mu\text{m}$. The cell area is 274.4 cm^2 .

Corrosion resistance experiment

The corrosion resistance experiment of TCO films mainly simulates the corrosion of films by plating solution and stripping solution in electroplating processes, and the corresponding verification is the acid and alkali resistance of the films. Among them, plating solution is mainly composed of cupric sulfate, sulfuric acid and chloride ion, at concentration of 120 g l^{-1} , 150 g l^{-1} and 60 ppm , respectively. Stripping solution includes saccharin sodium and sodium hydroxide, at concentration of 50 g l^{-1} and 1 g l^{-1} , respectively. According to the electroplating process, TCO films were soaked for 12 min and 160 s in plating solution and stripping solution, respectively, at room temperature and 50–65 °C. After soaking in solution, TCO films were rinsed with deionized water and blown dry, and then basic photoelectric properties were tested.

Characterization

The structural properties were measured by XRD (D8 ADVANCE, Bruker) using $\text{Cu K}\alpha$ radiation in the conventional 2θ – θ test mode. Surface images of the films were detected by AFM (Dimension XR, Bruker). PL spectra were measured by using a fluorescence spectrometer (BT Imaging R2 Plus) at room temperature. The composition of the samples was determined by XPS (ESCALAB Xi+, Thermo Fisher) using $\text{Mg K}\alpha$ ($1,253.6 \text{ eV}$) radiation. The transmittance and reflectance spectra were measured by using a spectrophotometer (LAMBDA 1050, PerkinElmer). The thickness of the films was measured by using an ellipsometer (SE 800 PV, Sentech). The sheet resistance was measured by the four-point probe method. The contact resistivity of SHJ solar cells was calculated using the Cox and Strack method. The spectral response of the fabricated SHJ solar cells was studied by quantum efficiency (PVE300-IVT, Bentham Instruments) spectra.

Reporting summary

Further information on research design is available in the Nature Portfolio Reporting Summary linked to this article.

Data availability

All data generated or analysed during this study are included in the published article and its Supplementary Information. Source data are provided with the paper. Any additional information is available from corresponding authors upon request.

References

- Wakisaka, K. et al. More than 16% solar cells with a new ‘HIT’ (doped a-Si/nondoped a-Si/crystalline Si) structure. *Conf. Rec. Twenty-Second IEEE Photovolt. Specialists Conf.-1991* **2**, 887–892 (1991).
- Yoshikawa, K. et al. Silicon heterojunction solar cell with interdigitated back contacts for a photoconversion efficiency over 26%. *Nat. Energy* **2**, 17032 (2017).
- Razzaq, A., Allen, T. G., Liu, W., Liu, Z. & De Wolf, S. Silicon heterojunction solar cells: techno-economic assessment and opportunities. *Joule* **6**, 514–542 (2022).
- Cruz, A. et al. Optoelectrical analysis of TCO+silicon oxide double layers at the front and rear side of silicon heterojunction solar cells. *Sol. Energy Mater. Sol. Cells* **236**, 111493 (2022).
- Favier, A., Munoz, D., De Nicolás, S. M. & Ribeyron, P. J. Boron-doped zinc oxide layers grown by metal-organic CVD for silicon heterojunction solar cells applications. *Sol. Energy Mater. Sol. Cells* **95**, 1057–1061 (2011).
- Yu, J. et al. Copper metallization of electrodes for silicon heterojunction solar cells: process, reliability and challenges. *Sol. Energy Mater. Sol. Cells* **224**, 110993 (2021).
- Minami, T., Suzuki, S. & Miyata, T. Transparent conducting impurity-co-doped ZnO:Al thin films prepared by magnetron sputtering. *Thin Solid Films* **398**, 53–58 (2001).
- Min, H. et al. Perovskite solar cells with atomically coherent interlayers on SnO_2 electrodes. *Nature* **598**, 444–450 (2021).
- Liu, Z. et al. A holistic approach to interface stabilization for efficient perovskite solar modules with over 2,000-hour operational stability. *Nat. Energy* **5**, 596–604 (2020).
- Liu, M. et al. SnO_2/Mg combination electron selective transport layer for Si heterojunction solar cells. *Sol. Energy Mater. Sol. Cells* **200**, 109996 (2019).
- Wang, Q. et al. p-Type c-Si/ SnO_2/Mg heterojunction solar cells with an induced inversion layer. *Appl. Phys. Lett.* **119**, 263502 (2021).
- Yang, G. et al. Defect engineering in wide-bandgap perovskites for efficient perovskite–silicon tandem solar cells. *Nat. Photonics* **16**, 588–594 (2022).
- Al-Ashouri, A. et al. Monolithic perovskite/silicon tandem solar cell with > 29% efficiency by enhanced hole extraction. *Science* **370**, 1300–1309 (2020).
- Szuber, J., Czempik, G., Larciprete, R., Koziej, D. & Adamowicz, B. XPS study of the L-CVD deposited SnO_2 thin films exposed to oxygen and hydrogen. *Thin Solid Films* **39**, 198–203 (2001).
- Luo, H., Liang, L. Y., Cao, H. T., Liu, Z. M. & Zhuge, F. Structural, chemical, optical, and electrical evolution of SnO_x films deposited by reactive rf magnetron sputtering. *ACS Appl. Mater. Interfaces* **4**, 5673–5677 (2012).
- Gu, F. et al. Luminescence of SnO_2 thin films prepared by spin-coating method. *J. Cryst. Growth* **262**, 182–185 (2004).
- Vanheusden, K., Warren, W. L., Seager, C. H., Tallant, D. R. & Voigt, J. A. Mechanisms behind green photoluminescence in ZnO phosphor powders. *J. Appl. Phys.* **79**, 7983–7990 (1996).
- Trani, F., Causà, M., Ninno, D., Cantele, G. & Barone, V. Density functional study of oxygen vacancies at the SnO_2 surface and subsurface sites. *Phys. Rev. B* **77**, 245410 (2008).
- Tao, Y., Zhu, B., Yang, Y., Wu, J. & Shi, X. The structural, electrical, and optical properties of SnO_2 films prepared by reactive magnetron sputtering: Influence of substrate temperature and O_2 flow rate. *Mater. Chem. Phys.* **250**, 123129 (2020).
- Li, S. et al. Transparent-conductive-oxide-free front contacts for high-efficiency silicon heterojunction solar cells. *Joule* **5**, 1535–1547 (2021).
- Dong, G. et al. Power conversion efficiency of 25.26% for silicon heterojunction solar cell with transition metal element doped indium oxide transparent conductive film as front electrode. *Prog. Photovolt. Res. Appl.* **30**, 1136–1143 (2022).
- Yu, J. et al. Copper metallization of electrodes for silicon heterojunction solar cells: process, reliability and challenges. *Sol. Energy Mater. Sol. Cells* **224**, 110993 (2021).

Acknowledgements

We thank L. Lv, H. Wu, C. He, Y. Sun and H. Wu for sample fabrication and testing. X.Z. acknowledges financial support from the National Natural Science Foundation of China (grant nos. U21A2072 and 62274099) and the Fundamental Research Funds for the Central Universities (Nankai University). J.Z. and X.C. acknowledge financial support from the Carbon Emission Peak and Carbon Neutrality Special Fund of Jiangsu Province (BA2022205). We acknowledge Haihe Laboratory of Sustainable Chemical Transformations.

Author contributions

These authors contributed equally: C.Y. and Q.Z. G.D. and X.Z. conceived and directed the overall project. C.Y. and G.D. fabricated all the devices and conducted the characterization. V.A. prepared electroplated copper electrodes and carried out related work. Q.Z. characterized and analysed the materials with the assistance of G.D. and X.Z. Q.Z., Y.Z., X.R., C.-W.P., Q.W., V.A., X.C. and J.Z. contributed to useful discussions. C.Y., Q.Z., G.D. and X.Z. wrote the paper. All authors discussed the results and commented on the paper.

Competing interests

C.Y., Q.W., Y.Z., X.R., G.D., C.-W.P., X.C. and J.Z. are employees of Suzhou Maxwell Technologies Co., Ltd. V.A. is an employee of SunDrive Solar Pty., Ltd. The other authors declare no competing interests.

Additional information

Supplementary information The online version contains supplementary material available at <https://doi.org/10.1038/s41560-023-01331-7>.

Correspondence and requests for materials should be addressed to Gangqiang Dong or Xiaodan Zhang.

Peer review information *Nature Energy* thanks Martin Bivour and the other, anonymous, reviewer(s) for their contribution to the peer review of this work.

Reprints and permissions information is available at www.nature.com/reprints.

Publisher's note Springer Nature remains neutral with regard to jurisdictional claims in published maps and institutional affiliations.

Springer Nature or its licensor (e.g. a society or other partner) holds exclusive rights to this article under a publishing agreement with the author(s) or other rightsholder(s); author self-archiving of the accepted manuscript version of this article is solely governed by the terms of such publishing agreement and applicable law.

© The Author(s), under exclusive licence to Springer Nature Limited 2023

Solar Cells Reporting Summary

Nature Research wishes to improve the reproducibility of the work that we publish. This form is intended for publication with all accepted papers reporting the characterization of photovoltaic devices and provides structure for consistency and transparency in reporting. Some list items might not apply to an individual manuscript, but all fields must be completed for clarity.

For further information on Nature Research policies, including our [data availability policy](#), see [Authors & Referees](#).

► Experimental design

Please check: are the following details reported in the manuscript?

1. Dimensions

Area of the tested solar cells	<input checked="" type="checkbox"/> Yes	274.4 square centimeter
	<input type="checkbox"/> No	
Method used to determine the device area	<input checked="" type="checkbox"/> Yes	The area of the calibration object is measured using an optical scanning system working in transmission mode and is traceable to a primary calibrated area standard (Calibration mark 50716-PTB-19 (FN001)), stated in Calibration certificate.
	<input type="checkbox"/> No	

2. Current-voltage characterization

Current density-voltage (J-V) plots in both forward and backward direction	<input type="checkbox"/> Yes	Forward direction is enough for our SHJ solar cells.
	<input checked="" type="checkbox"/> No	
Voltage scan conditions <i>For instance: scan direction, speed, dwell times</i>	<input checked="" type="checkbox"/> Yes	Forward direction; 400 points; Scan time 1s.
	<input type="checkbox"/> No	
Test environment <i>For instance: characterization temperature, in air or in glove box</i>	<input checked="" type="checkbox"/> Yes	All devices were tested under standard conditions (AM1.5G, 25 degrees Celsius).
	<input type="checkbox"/> No	
Protocol for preconditioning of the device before its characterization	<input type="checkbox"/> Yes	There is no preconditioning.
	<input checked="" type="checkbox"/> No	
Stability of the J-V characteristic <i>Verified with time evolution of the maximum power point or with the photocurrent at maximum power point; see ref. 7 for details.</i>	<input type="checkbox"/> Yes	Not relevant.
	<input checked="" type="checkbox"/> No	

3. Hysteresis or any other unusual behaviour

Description of the unusual behaviour observed during the characterization	<input type="checkbox"/> Yes	Silicon cells do not exhibit hysteresis under standard conditions.
	<input checked="" type="checkbox"/> No	
Related experimental data	<input type="checkbox"/> Yes	Silicon cells do not exhibit hysteresis under standard conditions.
	<input checked="" type="checkbox"/> No	

4. Efficiency

External quantum efficiency (EQE) or incident photons to current efficiency (IPCE)	<input checked="" type="checkbox"/> Yes	Fig. 2d and supplement Fig. 10b
	<input type="checkbox"/> No	
A comparison between the integrated response under the standard reference spectrum and the response measure under the simulator	<input type="checkbox"/> Yes	Certificate reports do not contains this comparison.
	<input checked="" type="checkbox"/> No	
For tandem solar cells, the bias illumination and bias voltage used for each subcell	<input type="checkbox"/> Yes	They are not tandem solar cells.
	<input checked="" type="checkbox"/> No	

5. Calibration

Light source and reference cell or sensor used for the characterization	<input checked="" type="checkbox"/> Yes	Class AAA light source; The reference cell was calibrated and certified in ISFH.
	<input type="checkbox"/> No	
Confirmation that the reference cell was calibrated and certified	<input checked="" type="checkbox"/> Yes	The reference cell was calibrated and certified in ISFH.
	<input type="checkbox"/> No	

Calculation of spectral mismatch between the reference cell and the devices under test

☐ Yes
☒ No

Certificate report does not contains this mismatch comparison.

6. Mask/aperture

Size of the mask/aperture used during testing

☐ Yes
☒ No

We tested solar cells without the mask/aperture. A full area test was used.

Variation of the measured short-circuit current density with the mask/aperture area

☐ Yes
☒ No

Not relevant.

7. Performance certification

Identity of the independent certification laboratory that confirmed the photovoltaic performance

☒ Yes
☐ No

Institut für Solarenergieforschung Hameln (ISFH)

A copy of any certificate(s)

Provide in Supplementary Information

☒ Yes
☐ No

Fig. 3c

8. Statistics

Number of solar cells tested

☒ Yes
☐ No

The number of solar cells is indicated in the manuscript.

Statistical analysis of the device performance

☒ Yes
☐ No

supplement Fig. 9, supplement Fig. 11 and supplement Fig. 12

9. Long-term stability analysis

Type of analysis, bias conditions and environmental conditions

For instance: illumination type, temperature, atmosphere humidity, encapsulation method, preconditioning temperature

☐ Yes
☒ No

Long-term stability analysis has not yet been performed.